Supporting Information

Tanner et al. 10.1073/pnas.1119578109

SI Materials and Methods

Molecular Cloning and Lentiviral Expression. Human mammary epithelial cell (HMEC) lines S1 and T4-2 (HMT3522) (1–3), and MCF10A (4) were cultured as previously described. H2B-GFP (5) plasmid was purchased from Addgene (Cat#11680) and the insert was cleaved and cloned into pLentiCMV/TO-Neo, kindly provided by Alvin T. Lo (Lawrence Berkeley National Laboratory, Berkeley, CA). For lentiviral production, pLenti-CMV/TO-Neo H2B-GFP was cotransfected with pLP1, pLP2, and pLP-VSVG helper plasmids (Invitrogen) into 293FT host cells using Fugene6 transfection reagent (Roche) and the supernatant collected for viral transduction. S1, T4-2, and MCF10A cells were infected with viral supernatants in the presence of 4 mg/mL polybrene, and cell lines were stably selected with neomycin, subsequently infected with mCherry LifeAct (6) viral supernatant, and stably selected with puromyocin.

Partitioning deficient 3 homolog (PAR3) knock-down was performed with PARD3 shRNA (Santa Cruz Biotechnologies), and cells with stably expressing shRNA were selected with puromyocin.

Cell Culture and Sample Preparation. Normal primary human breast epithelial cells (N120, passage 1) were a kind gift from William Curt Hines, (Lawrence Berkeley National Laboratory, Berkeley, CA) obtained from the University of California at San Francisco Cancer Center and the Cooperative Human Tissue Network. N120 cells were isolated from tissue obtained from reduction mammoplasties as previously described (7, 8). HMT3522 and MCF10a series (10a, 10aT, and CA1) cell lines were cultured in 3D on covered glass chambers with a coverslip-bottomed no. 1.0 (Nalge Nunc) according to previously described methods (2–4). Phenotypic reversion of T4-2 cells was achieved by either using β1 integrin function-blocking (AIIB2) or EGFR inhibitor (Tyrphostin, AG1478), as previously described (3, 9, 10).

After isolation, primary HMEC were either (*i*) embedded as single cells in lrECM (BD Biosciences Matrigel) and allowed to form acini (8 d) or (*ii*) preaggregated by centrifuging at 200 × *g* and resuspended without disassociation in laminin-rich gels (lrECM). Each preparation was then immediately placed at 37 °C to facilitate gelation for 30 min. Complete medium was then added to the cultures and replenished every 2 d. For live imaging, cell dye ER-tracker-mCherry (Invitrogen) specific for the endoplasmic reticulum was added to the medium at a final concentration of 1:1,000 for 30 min. Samples were replenished with fresh media before imaging. Dye was maintained as cells divided, resulting in the presence of dye in progeny.

Pharmalogical and Antibody Treatment. The 3D cultures were pretreated with either 5 μM Y-27632 (Calbiochem), 25 μM Blebbistatin, 0.5 μM ML-7 (Sigma), 200 μg/mL mouse anti–E-Cadherin, or anti-IgG (Human; Invitrogen), respectively, for 2 h before imaging by supplementing lrECM/medium suspension, where the final concentration was 5% lrECM (vol/vol). This treatment was repeated when media was refreshed at day 3 of 3D culture. At day 5, samples were fixed and stained according to previously described methodology (11, 12) for F-actin (Alexa 594 phalloidin), phospho-myosin light chain 2 (pMLC), Thr18/Ser19 (Antibody #3674, Cell Signaling), or E-Cadherin (BD Transduction Lab), secondary antibody Alexa 488, and DNA (DAPI). Cells were harvested also from lrECM for immunoprecipitation as previously described (10). Immunoblots of cell lysates were probed for pMLC, MLC (Antibodies cat. #3674 and #3672; Cell Signaling), PARD3 (Abcam; ab64840) and internal control, Lamin A/C. For live imaging, the cell dye was ER-tracker-mCherry (Invitrogen).

Imaging Parameters. ***Immunofluorescence.*** Images were acquired at a frame-rate of ∼one per second with an upright Zeiss LSM 710 Meta confocal microscope. One-photon, confocal 3D dimensional images of 512 × 512 pixels (lateral dimensions), where the maximum axial displacement measured was 75 μm, were acquired with a 1.4 NA 63× oil-immersion objective corresponding to an area of 134.9 × 134.9 μm^2. Images were acquired in incremental steps of 0.5 μm in the axial direction. Samples were imaged sequentially with the 405 nm and 488 nm (respectively) lines from an argon ion laser with a power of <3% (total power 30 mW) and 546 nm from a solid-state laser (power of <10%). Band-pass filters were set in the emission pathway for blue (band-pass filter 450–465), green (band-pass filters 505–525 nm), and red (560–575 nm), and channels at a gain of 400 on the amplifier. For each channel, the pinhole was set to 1 Airy unit.
Live cell imaging. Three-dimensional images as a function of time were also obtained with a Zeiss LSM 710 Meta confocal microscope. Images of dimensions, 512 × 512 pixels (lateral dimensions) with a maximum axial displacement of 75 μm (axial step size, 2 μm) were acquired using a 0.8 NA 20× air objective at digital zoom of 0.6, corresponding to an area of 701 × 701 μm^2 at a rate of ∼one frame per second. A time interval of 20 min was programmed between successive frames for 4 d. Settings were tuned to simultaneous excitation of the 488-nm line from an argon ion laser with a power of <3% (total power 30 mW) and 546 nm from a solid-state laser (power of <10%). A secondary dichroic mirror, SDM 560, was used in the emission pathway to separate the red (band-pass filters 560–575 nm) and green (band-pass filters 505–525 nm) channels, at a gain of 400 on the amplifier an image acquisition rate of one frame per second. The laser power for the 543-nm setting was set at <3% of the maximum power and the gain on the detectors was set to 450. Samples were maintained at 37 °C and 5% CO_2.
Image processing. Immunofluorescence images for each focal plane were exported using Zen 2009 (Zeiss) software and ImageJ for display. Three-dimensional volume rendering and individual cell tracking were performed using object-tracking and volume-rendering algorithms in Bitplane Imaris software. For multicellular structures, individual cell traces were exported for periods excluding mitosis and the angular velocity and mean square displacement were calculated.

Sphericity. Sphericity is a measure of how spherical an object is; thus, it provides a measure of compactness for a given shape (13). The sphericity, Ψ, of a particle is the ratio of the surface area of a sphere (with the same volume as the given particle) to the surface area of the particle.

$$\Psi = \frac{\pi^{\frac{1}{3}}(6V_p)^{\frac{2}{3}}}{A_p} \qquad [S1]$$

where V_p is volume of the particle and A_p is the surface area of the particle.

Mean Square Displacement and Cell Tracking. Trajectories of single-cell and geometric center of multicellular structures were analyzed in a similar manner to that described by Saxton and Jacobson (14), where the particle motion was extended to three

dimensions (x, y, z). We calculated the mean-square displacement (MSD) as a function of a lag time (τ) for lags corresponding to one-quarter of the total datapoints:

$$\mathrm{MSD}(\tau) = \left\langle \left(x(t) - x(t+\tau)\right)^2 + \left(y(t) - y(t+\tau)\right)^2 + \left(z(t) - z(t+\tau)\right)^2 \right\rangle. \quad [S2]$$

To quantitatively analyze the motion of the particles, we apply the following fitting parameters to the trajectories (14).

$$\mathrm{MSD}(\tau) = 6D\tau \quad [S3]$$

$$\mathrm{MSD}(\tau) = 6D\tau + (v\tau)^2, \quad [S4]$$

where D is the diffusion coefficient and v is velocity.

These equations consider normal random diffusion (Eq. **S3**), and directed motion with diffusion (Eq. **S4**) in three dimensions. These models were fitted to the experimental data, and the best-fitting model provides the parameters D and v, for the cellular motion.

Statistical Analysis. Statistical comparisons were performed using the statistical toolbox of Graphpad Prism.

Bar graphs are shown as mean with SEs for trajectory analysis as the distributions were Gaussian and a Student t test (unpaired, two-tailed, 95% confidence interval) was used to determine if these distributions were statistically significantly different.

For sphericity analysis, distributions were not Gaussian (as confirmed by the Bartlett's test); we compared the distributions using nonparametric methods. We compared whether the median values of the two samples were significantly different ($P < 0.01$) using the two-sided Mann–Whitney test.

1. Briand P, Petersen OW, Van Deurs B (1987) A new diploid nontumorigenic human breast epithelial cell line isolated and propagated in chemically defined medium. *In Vitro Cell Dev Biol* 23:181–188.
2. Petersen OW, Rønnov-Jessen L, Howlett AR, Bissell MJ (1992) Interaction with basement membrane serves to rapidly distinguish growth and differentiation pattern of normal and malignant human breast epithelial cells. *Proc Natl Acad Sci USA* 89: 9064–9068.
3. Lee GY, Kenny PA, Lee EH, Bissell MJ (2007) Three-dimensional culture models of normal and malignant breast epithelial cells. *Nat Methods* 4:359–365.
4. Debnath J, Muthuswamy SK, Brugge JS (2003) Morphogenesis and oncogenesis of MCF-10A mammary epithelial acini grown in three-dimensional basement membrane cultures. *Methods* 30:256–268.
5. Kanda T, Sullivan KF, Wahl GM (1998) Histone-GFP fusion protein enables sensitive analysis of chromosome dynamics in living mammalian cells. *Curr Biol* 8:377–385.
6. Tanner K, Boudreau A, Bissell MJ, Kumar S (2010) Dissecting regional variations in stress fiber mechanics in living cells with laser nanosurgery. *Biophys J* 99:2775–2783.
7. Stampfer M, Hallowes RC, Hackett AJ (1980) Growth of normal human mammary cells in culture. *In Vitro* 16:415–425.
8. Mukhopadhyay R, et al. (2010) Promotion of variant human mammary epithelial cell outgrowth by ionizing radiation: An agent-based model supported by in vitro studies. *Breast Cancer Res* 12:R11.
9. Rizki A, et al. (2008) A human breast cell model of preinvasive to invasive transition. *Cancer Res* 68:1378–1387.
10. Wang F, et al. (1998) Reciprocal interactions between beta1-integrin and epidermal growth factor receptor in three-dimensional basement membrane breast cultures: A different perspective in epithelial biology. *Proc Natl Acad Sci USA* 95:14821–14826.
11. Weaver VM, et al. (1997) Reversion of the malignant phenotype of human breast cells in three-dimensional culture and in vivo by integrin blocking antibodies. *J Cell Biol* 137:231–245.
12. Lelièvre SA, et al. (1998) Tissue phenotype depends on reciprocal interactions between the extracellular matrix and the structural organization of the nucleus. *Proc Natl Acad Sci USA* 95:14711–14716.
13. Wadell H (1935) Volume, shape, and roundness of quartz particles. *J Geol* 43:250–280.
14. Saxton MJ, Jacobson K (1997) Single-particle tracking: Applications to membrane dynamics. *Annu Rev Biophys Biomol Struct* 26:373–399.

Micrographs of representative images for acini evolved from single primary epithelial cells

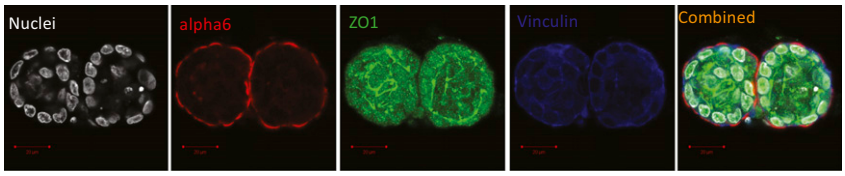

Fig. S1. Acinar structures complete with lumen are observed after 10 d of culture for normal human primary epithelial cells. Micrographs of representative images for acini evolved from single normal primary epithelial cells seeded as single cells isolated from tissue excised during a reduction mammoplasty. Immunofluorescence showing spatial localization of the nuclei (DAPI-gray), α-6 integrin (basal polarity-red), ZO-1 (tight junctions-green), Vinculin (blue), and the combined channels.

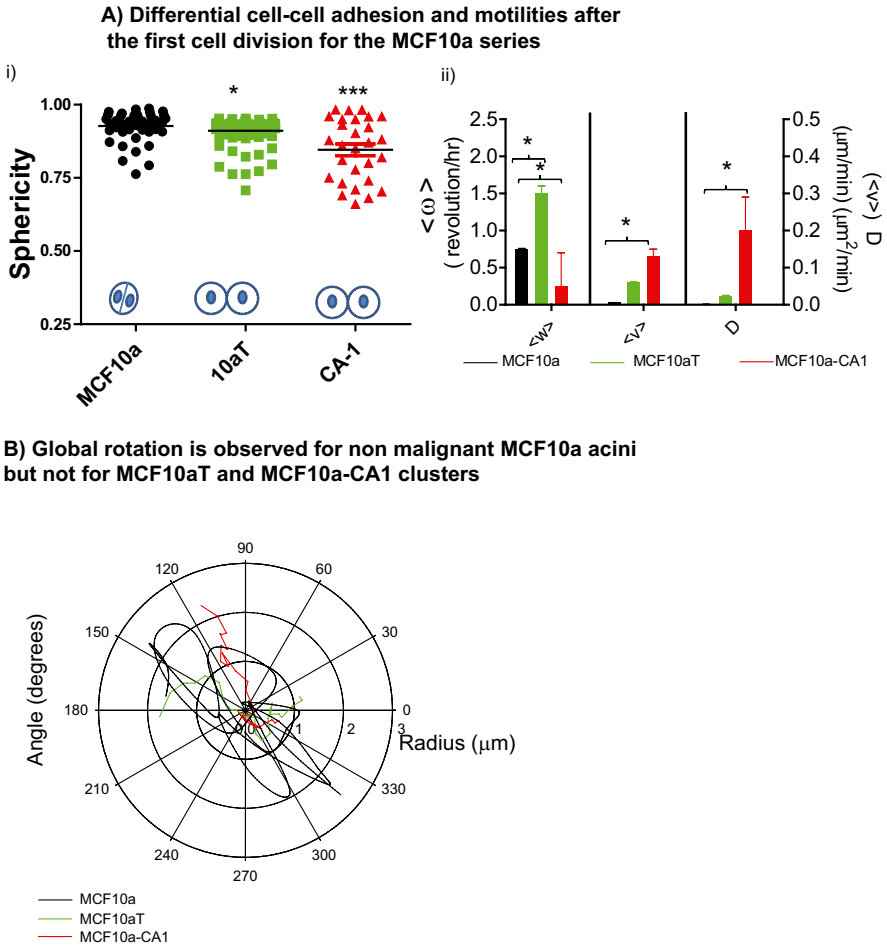

Fig. S2. Differential cell-cell adhesion and motilities after the first cell division for the human mammary epithelial cell MCF10a series. (*A*, *i*) Comparison of cell adhesion measured by sphericity of the cell aggregates for MCF10a series showing the relative changes of shape as a function of malignancy after the first cell division (two-cell stage) in early-stage 3D culture.. Sphericity of ∼1 indicates that cells have strong cell-cell adhesion; decrease in this value reflects that the cells are not tightly bound and the aggregate is no longer spherical. ***$P < 0.0001$ and *$P < 0.01$. (*ii*) Graphs showing the quantification as early as the first cell division during acinar morphogenesis; the distinction between nonmalignant and malignant is evident in the rotation of the cells: MCF10a multiple rotations whereas the premalignant MCF10aT T4-2 cells no longer rotate but instead show a combination of linear velocity as well as random motion (<v> and D respectively). Asterisks indicate *P* value as obtained using Student *t* test (unpaired, two-tailed, 95% confidence interval), where *$P < 0.01$. (*B*) Global rotation is observed for nonmalignant MCF10as but not for MCF10aT and MCF10a-CA1 clusters. Polar graph shows the coherent angular motion as demonstrated by tracking the geometric center as a function of time for MCF10a, MCF10aT, and MCF10a-CA1.

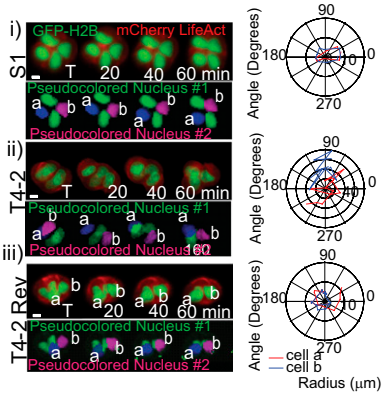

Fig. S3. Structural and migration differences observed after the first cell division for malignant T4-2, compared with the nonmalignant S1, are restored upon phenotypic reversion of T4-2 and is maintained for successive cell divisions. Micrographs of relative positions of nuclei as a function of time for S1 (*i*), T4-2 (*ii*), and T4-2 Rev (*iii*). The "a" and "b" are used to denote cells that were tracked for polar plots. Lower panel for each shows the pseudocolored nuclei.

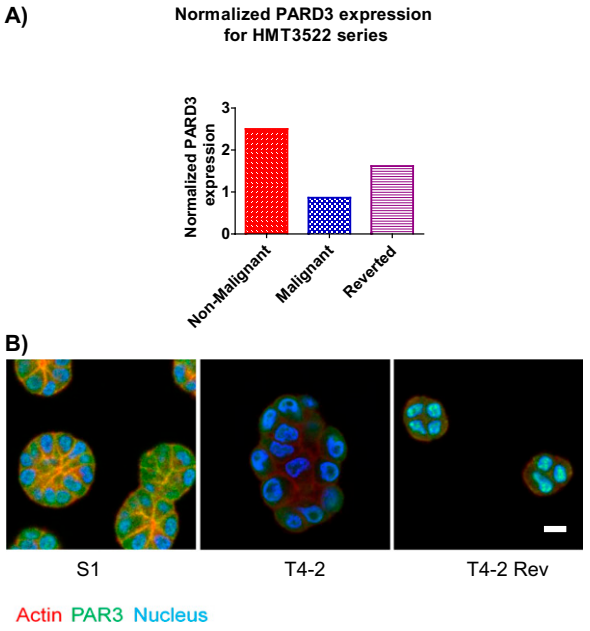

Fig. S4. Expression levels of PARD3 for the HMT3522 human cancer progression series. (*A*) Graph showing the relative gene expression of the PARD 3 levels for the HMT3522 series. (*B*) Micrographs showing the spatial localization using immunofluorescence of actin (red), PAR3 (green), and DNA (DAPI-blue) for the HMT3522 series. (Scale bar, 10 μm.)

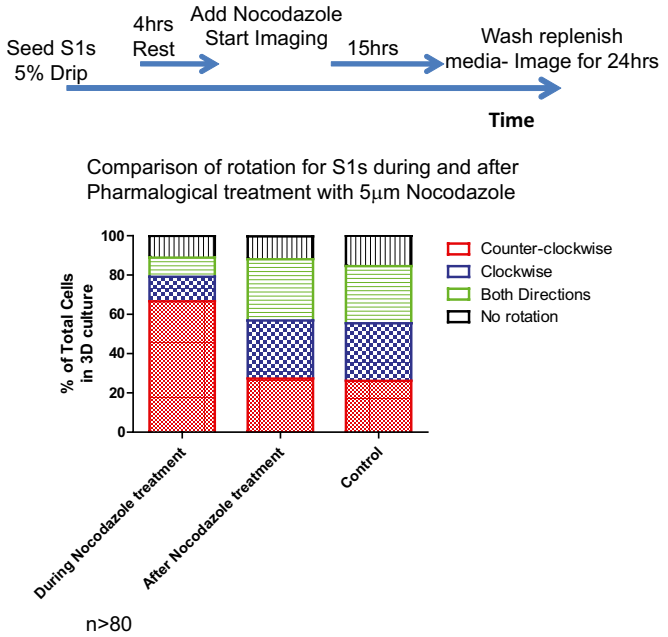

Fig. S5. Pharmacological destabilization of microtubules does not prevent single cell rotation for nonmalignant human mammary epithelial cells cells. (*Upper*) Schematic of experimental protocol. (*Lower*) Graph shows comparison of rotation for S1s during and after pharmacological treatment with 5 μm Nocodazole of the nonmalignant HMT3522-S1 cells in 3D culture.

Table S1. Mitotic dynamics for HMT3522 series, where ± sign is SEM

	Time between mitoses		
Cell type	First mitosis (1–2 cells)	Second mitosis (2–3 cells)	Third mitosis (3–4 cells)
S1	1343 (±35)	230 (±50)	237 (±48)
T4-2	437 (±38)	224 (±82)	57 (±25)
T4-2 AIIB2	1318 (±64)	613 (±74)	352 (±187)
T4-2 Tyrphostin	1830 (±201)	800 (±100)	600 (±150)

Table S2. Percentage of rotating structures after 5-d seeded in culture

Cell line	Percentage of rotating clusters
S1	76 (38/50)
T4-2	8 (4/50)
T4-2 tyrphostin	65 (33/50)
T4-2 AIIB2	62 (31/50)
MCF10a	70 (18/26)
MCF10aT	56 (18/32)
MCF10a-CA1	10 (2/21)

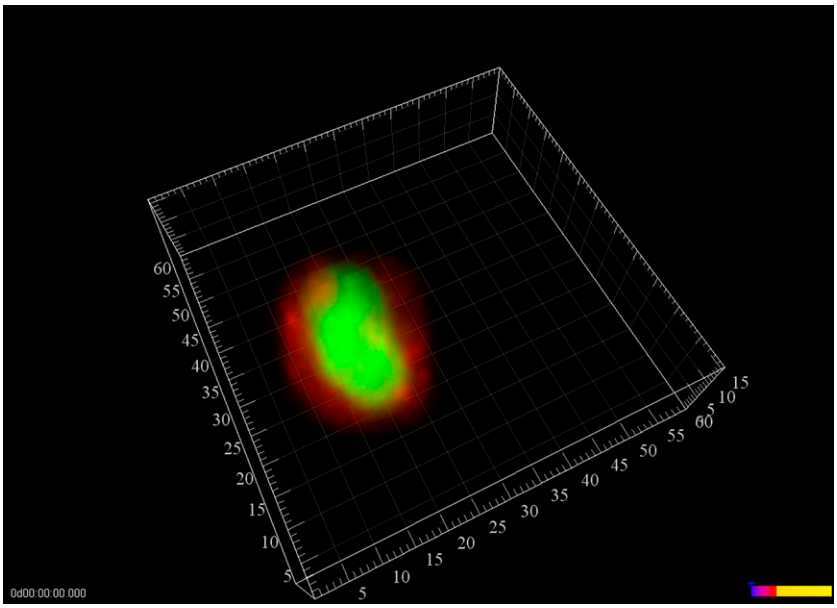

Movie S1. Acinar morphogenesis of HMT3522-S1, a non-malignant human breast epithelial cell line derived from reduction mammoplasty. Acinar morphogenesis in 3D laminin-rich gels (lrECM) was visualized with real-time fluorescence microscopy for 4 d. Coherent angular motion (CAMo) is observed as cells divide to form acini. For all movies, images were acquired at a rate of 1 frame/s with a time interval of 20 min between frames using real time confocal fluorescence microscopy. Playback rate is 30× the rate of acquisition.

Movie S1

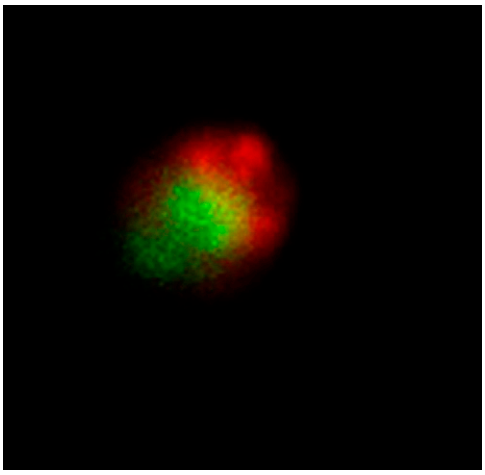

Movie S2. Acinar morphogenesis of MCF10A, a nonmalignant human breast epithelial cell line derived from reduction mammoplasty. Cell division of MCF10a cells during acinar morphogenesis in 3DlrECM shown for 12 hr.

Movie S2

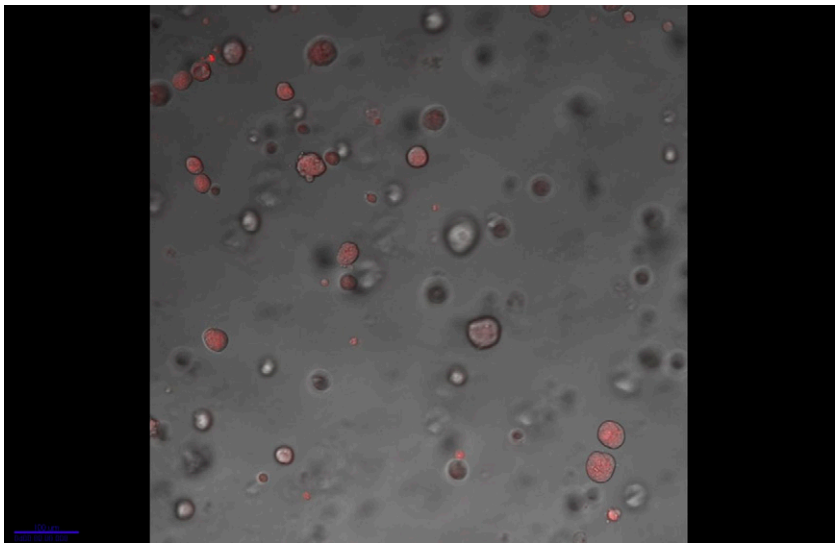

Movie S3. Single cell rotation of normal primary human breast epithelial cell. Wide view of single and small cell clusters at day 0 in 3D lrECM shown for 24 hr.

Movie S3

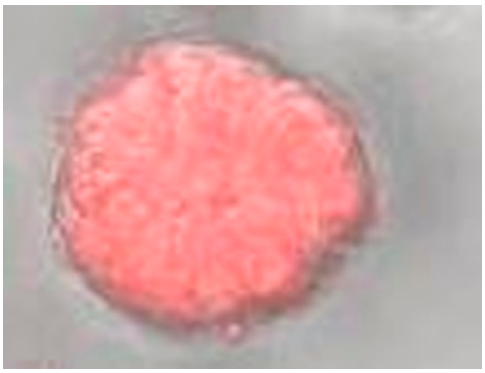

Movie S4. Acini derived from normal primary human breast epithelial cells undergo multiple rotations. CAMo continues to be present even after acini are formed; normal primary human breast epithelial cells visualized for 12 hr.

Movie S4

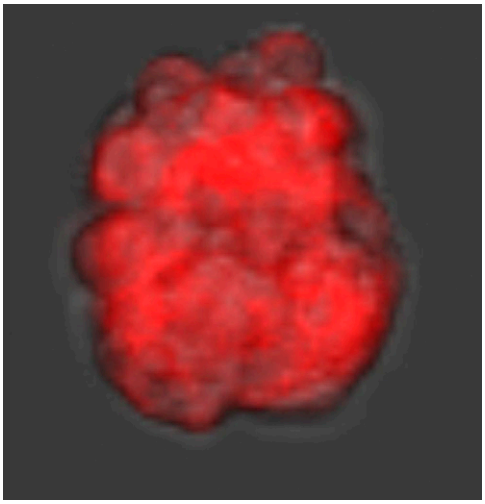

Movie S5. Aggregates derived from normal primary human breast epithelial cells display random motility. CAMo is not observed for multicellular aggregates of normal primary human breast epithelial cells shown for a period of 12 hr. These aggregates display random motility.

Movie S5

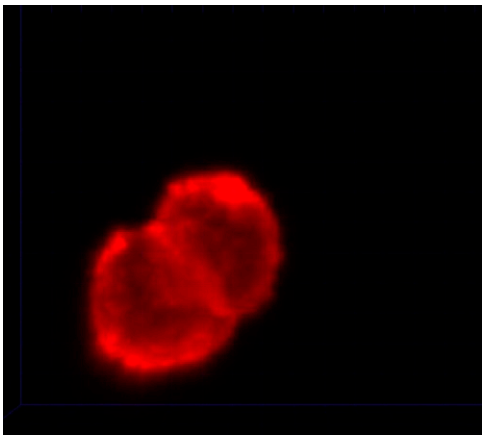

Movie S6. Evolution of malignant human epithelial cell, T4-2 in 3D-lrECM. Spatio-temporal evolution of T4-2 cells embedded in lrECM for 1 d shows symmetric division.

Movie S6

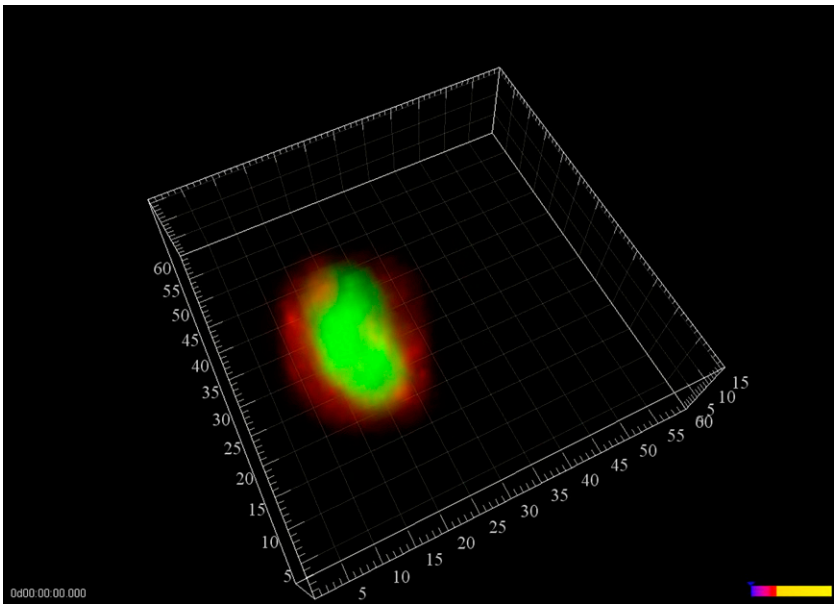

Movie S7. Acinar morphogenesis of non-malignant human epithelial cell, S1. Acinar morphogenesis of S1 cells acquired for 2 d showing CAMo is maintained as cells divide.

Movie S7

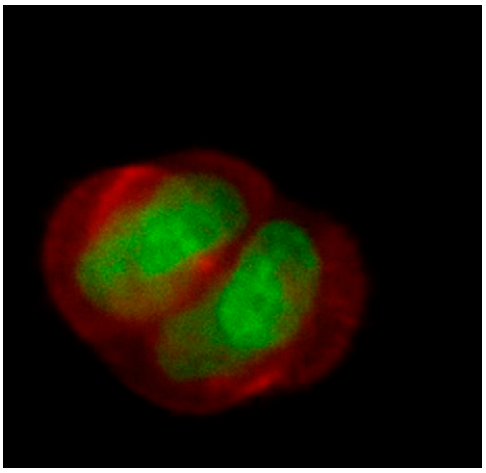

Movie S8. Malignant human breast epithelial cells, T4-2 show random motility after the first cell division. CAMo is no longer observed for T4-2 cells; image acquired for 12 hr. Instead, they show random, lateral motility.

Movie S8

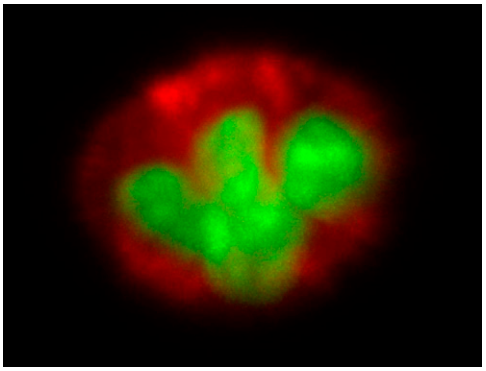

Movie S9. Phenotypically reverted- malignant T4-2 human epithelial cells (T4-2REV) undergo CAMo when placed in lrECM. CAMo is restored in T4-2 Rev cells; image acquired for 12 hr.

Movie S9

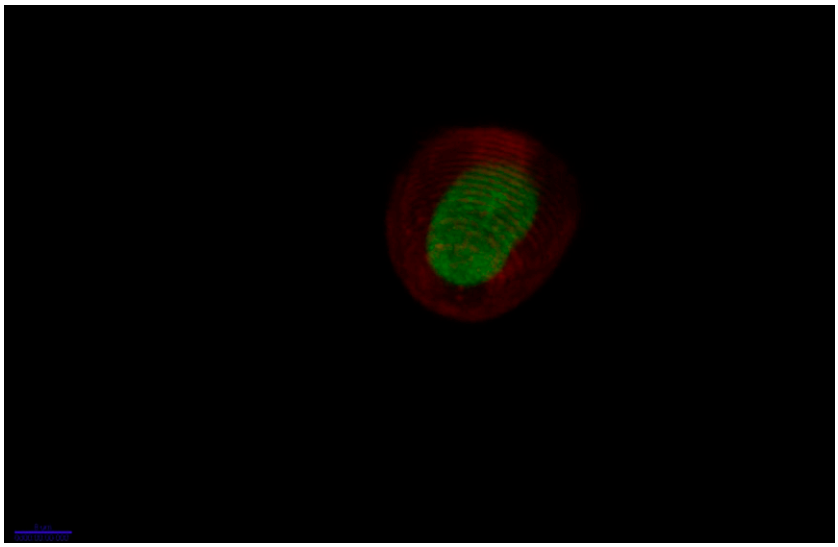

Movie S10. Acinar morphogenesis of non-malignant human epithelial cell, S1. Acinar morphogenesis of S1 cells acquired for 1 d showing CAMo is maintained as cells divide.

Movie S10

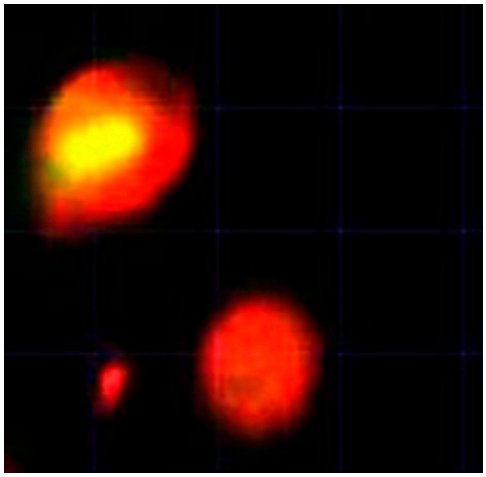

Movie S11. Malignant human breast epithelial cells, T4-2 show random motility during tumor formation. CAMo is no longer observed for T4-2 cells; image acquired for 2 d. Instead, they show random, lateral motility.

Movie S11

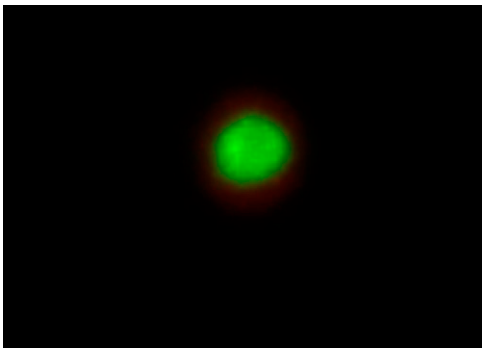

Movie S12. Acinar morphogenesis of T4-2 Rev-Tyrphostin. Acinar morphogenesis in 3D laminin-rich gels (lrECM) was visualized with real-time fluorescence microscopy for 4 d. Coherent angular motion (CAMo) is observed as cells divide to form acini.

Movie S12

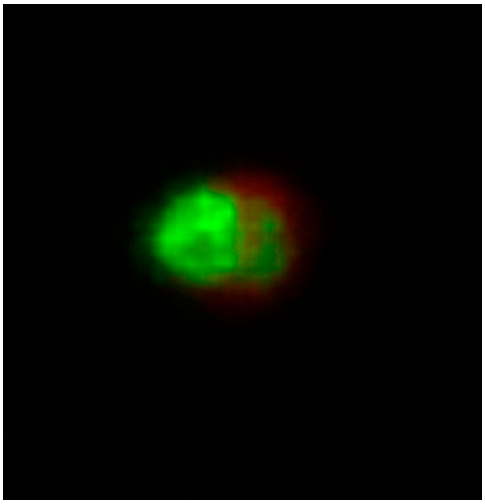

Movie S13. Acinar morphogenesis of T4-2 Rev-AIIB2. Acinar morphogenesis in 3D laminin-rich gels (lrECM) was visualized with real-time fluorescence microscopy for 4 d. Coherent angular motion (CAMo) is observed as cells divide to form acini.

Movie S13

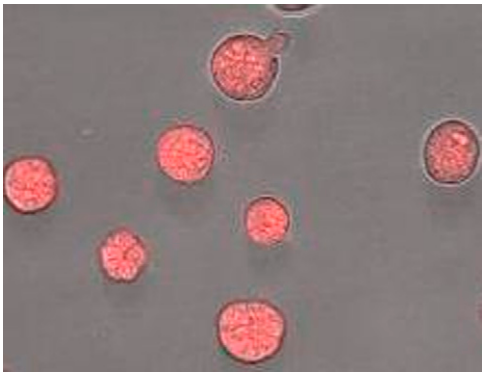

Movie S14. Clusters of Pre-Malignant human breast epithelial cells, MCF10aT show both CAMo and random motility. Mixed behavior is observed for MCF10aT where some acini show CAMo and others show random, lateral motility as observed at day 4 for 24 hr.

Movie S14

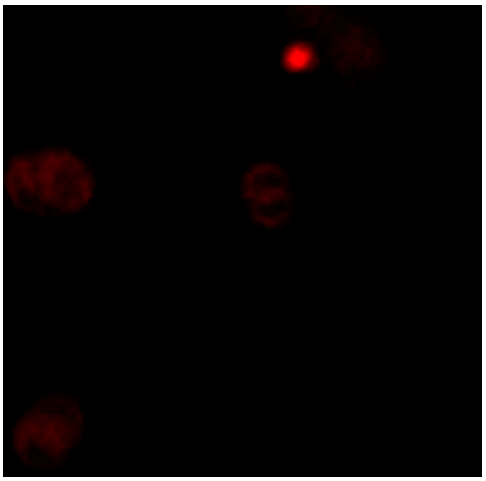

Movie S15. Clusters of Malignant human breast epithelial cells, MCF10a-CA1 show random motility. MCF10a-CA1 clusters show random, lateral motility as observed at day 4 for 24 hr.

Movie S15

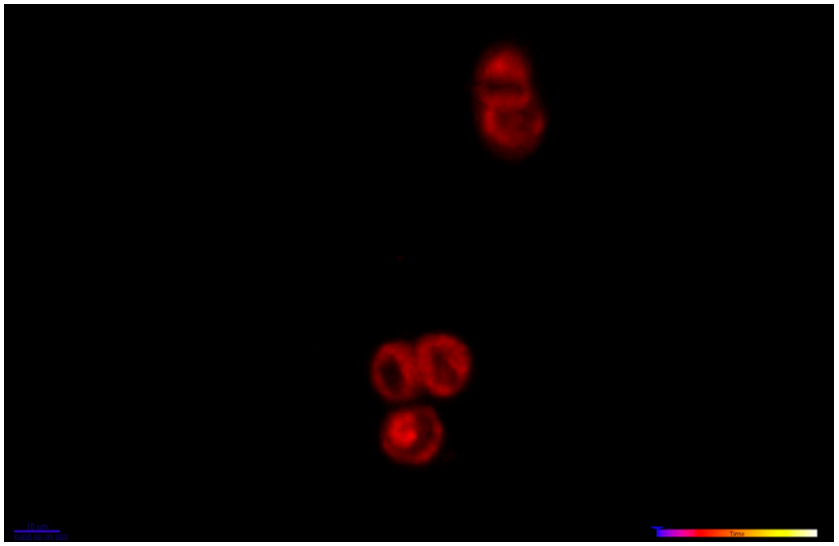

Movie S16. *PAR3* knock-down in S1 cells display compromised CAMo motility. Compromised CAMo motility is observed for S1 PAR3 knock-down cells at two cells stage during establishment of multicellular structures in 3D cultures, shown for 12 hr.

Movie S16

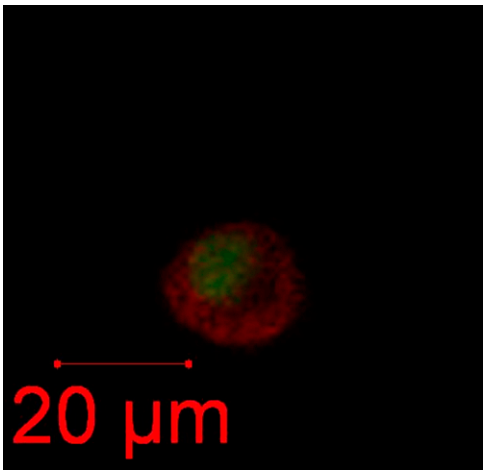

Movie S17. Single cell rotation showing circularly polarized peripheral actin. Single T4-2 cell at day 0 in 3D lrECM shown for 6 hr.

Movie S17

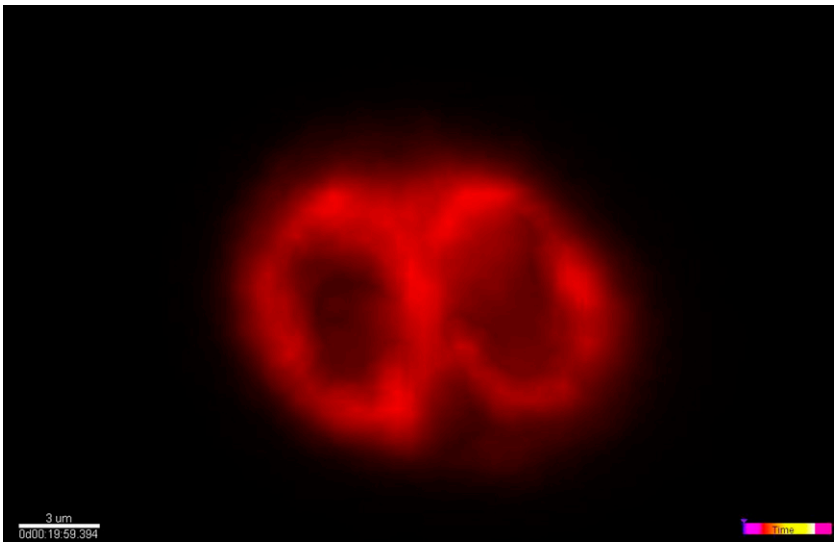

Movie S18. S1 control cells display CAMo motility. CAMo motility is observed for S1-untreated cells at the two cells stage during establishment of multicellular structure in 3D cultures shown for 12 hr.

Movie S18

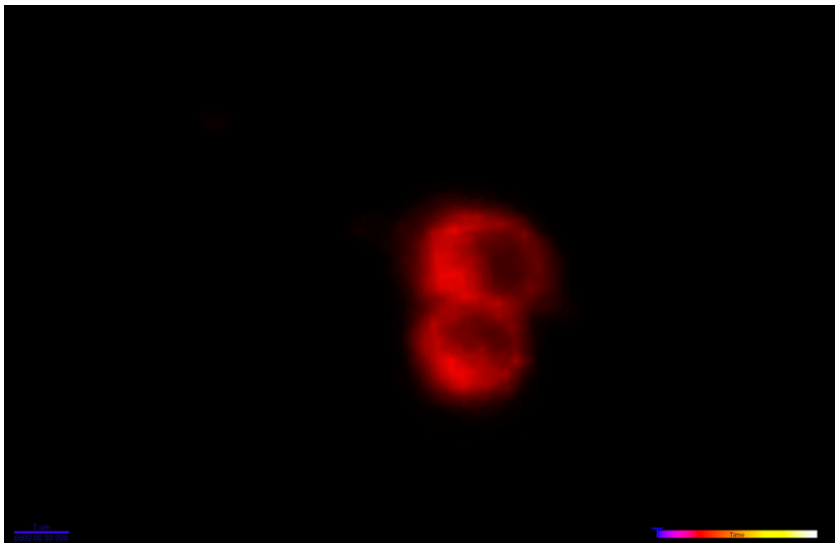

Movie S19. Loss of CAMo motility induced by Myosin II inhibition of S1 cells. CAMo motility is lost at the two cells stage during establishment of multicellular structure in 3D cultures when S1 cells are treated with 25 μM Blebbistatin shown for 12 hr.

Movie S19

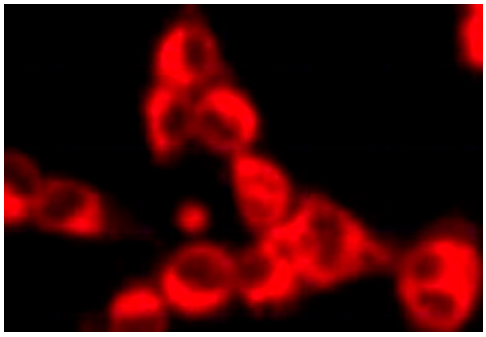

Movie S20. Loss of CAMo motility induced by Myosin II inhibition of S1 cells. Evolution of structures when S1 cells are treated with 25 μM Blebbistatin shown for 2 d where CAMo motility is lost at the two cells stage and maintained during establishment of multicellular structure in 3D .

Movie S20

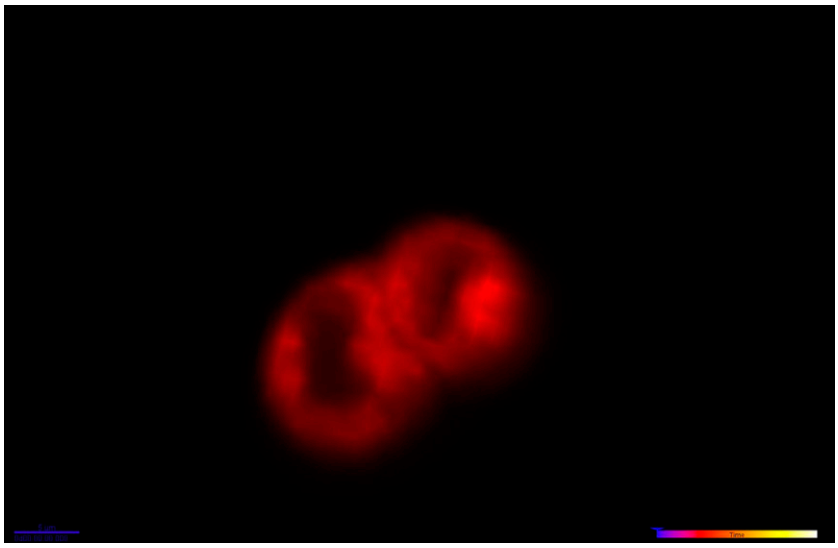

Movie S21. Loss of CAMo motility induced by MLCK inhibition of S1 cells. CAMo motility is lost at the two cells stage during establishment of multicellular structure in 3D cultures when S1 cells are treated with 0.5 μM ML-7 shown for 12 hr.

Movie S21

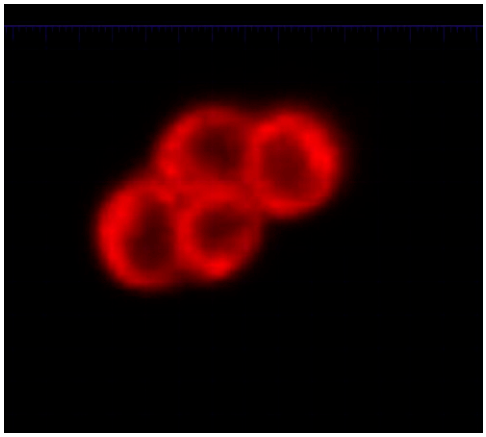

Movie S22. Loss of CAMo motility induced by MLCK inhibition of S1 cells. Evolution of structures when S1 cells are treated with 0.5 μM ML-7 shown for 2 d where CAMo motility is lost at the two cells stage and maintained during establishment of multicellular structure in 3D.

Movie S22

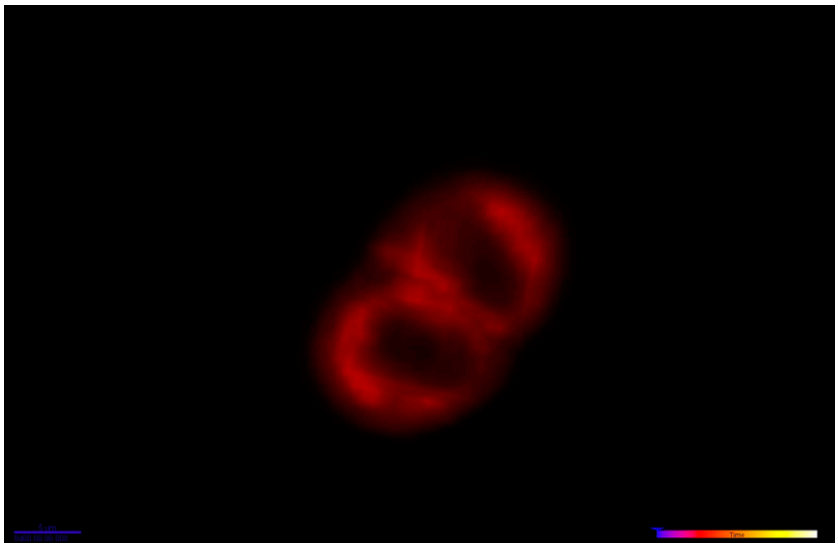

Movie S23. Loss of CAMo motility induced by ROCK inhibition of S1 cells. CAMo motility is lost at the two cells stage during establishment of multicellular structure in 3D cultures when S1 cells are treated with 5 μM Y-27632 shown for 12 hr.

Movie S23

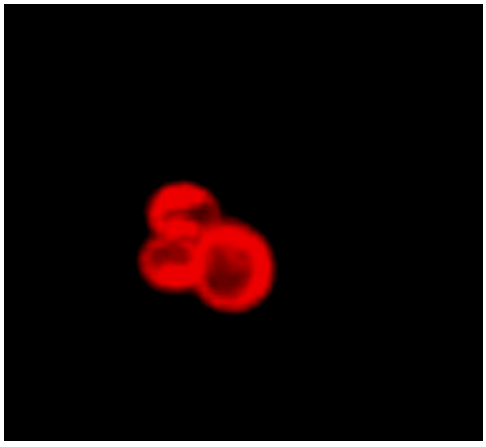

Movie S24. Loss of CAMo motility induced by ROCK inhibition of S1 cells. Evolution of structures when S1 cells are treated with 5 μM Y-27632 shown for 2 d where CAMo motility is lost at the two cells stage and maintained during establishment of multicellular structure in 3D.

Movie S24